

Postprint

This document is the Accepted Manuscript version of a Published Work that appeared in final form in
after peer review and technical editing by the publisher.

To access the final edited and published work see:

Access to the published version may require subscription.

When citing this work, please cite the original published paper.

Tailoring Bond Topologies in Open-shell Graphene Nanostructures

Shantanu Mishra,^{†,¶} Thorsten G. Lohr,^{‡,¶} Carlo A. Pignedoli,[†] Junzhi Liu,[‡] Reinhard Berger,[‡] José I. Urgel,[†] Klaus Müllen,[§] Xinliang Feng,^{‡,*} Pascal Ruffieux,[†] and Roman Fasel^{†,Δ,*}

[†]Empa, Swiss Federal Laboratories for Materials Science and Technology, Überlandstrasse 129, 8600 Dübendorf, Switzerland

[‡]Center for Advancing Electronics and Department of Chemistry and Food Chemistry, Technical University of Dresden, 01062 Dresden, Germany

[§]Max Planck Institute for Polymer Research, Ackermannweg 10, 55128 Mainz, Germany

^ΔDepartment of Chemistry and Biochemistry, University of Bern, Freiestrasse 3, 3012 Bern, Switzerland

KEYWORDS: scanning tunneling microscopy, scanning tunneling spectroscopy, open-shell polycyclic aromatic hydrocarbons, non-alternant polycyclic aromatic hydrocarbons, atom manipulation, density functional theory

ABSTRACT: Polycyclic aromatic hydrocarbons exhibit a rich spectrum of physico-chemical properties depending on the size, and more critically, on the edge and bond topologies. Among them, open-shell systems – molecules hosting unpaired electron densities – represent an important class of materials for organic electronic, spintronic and optoelectronic devices, but remain challenging to synthesize in solution. We report the on-surface synthesis and scanning tunneling microscopy- and spectroscopy-based study of two ultra-low-gap open-shell molecules, namely *peri*-tetracene, a benzenoid graphene fragment with zigzag edge topology, and dibenzo[*a,m*]dicyclohepta[*bcd,e,nop,q*]rubicene, a non-benzenoid non-alternant structural isomer of *peri*-tetracene with two embedded azulene units. Our results provide an understanding of the ramifications of altered bond topologies at the single-molecule scale, with the prospect of designing functionalities in carbon-based nanostructures *via* engineering of bond topology.

Topologies of the edge and the π -electron network are paramount in determining the electronic structure of nanographenes (or polycyclic aromatic hydrocarbons (PAHs)), and lead to exotic properties that are not present in the parent graphene. For example, the presence of zigzag edges leads to localized non-bonding edge states, wherein the resulting Coulomb instability *via* electron-electron interaction is relieved through spin polarization of the states.^{1,2} On the other hand, PAHs exhibiting distinctive π -electron topologies, such as triangular or bow-tie-shaped, inherently contain unpaired electrons as a result of unsatisfied atomic valencies arising from topological frustration in the bipartite lattice.³⁻⁵ Such systems belong to the family of open-shell PAHs, which has received increased interest in recent years due to potential applications in organic spintronics,⁶ non-linear optics⁷ and photovoltaics.⁸ The past decade has witnessed the realization of interesting classes of open-shell PAHs including zigzag graphene nanoribbons,⁹ acenes,¹⁰⁻¹³ anthenes,¹⁴ triangulene¹⁵ and post-graphene organic Dirac materials.^{16,17} However, their synthesis *via* solution-based chemistry remains challenging due to the high intrinsic reactivity arising from unpaired electron densities.¹⁸ In this regard, on-surface synthesis, utilizing surface-driven catalytic reactions of rationally-designed stable precursor

molecules under ultra-high vacuum (UHV) conditions, provides a valuable synthetic toolbox toward atomically-precise synthesis of PAHs hitherto unattainable *via* solution chemistry, and allows atomic-scale investigation of structural and electronic properties using scanning probe microscopies.¹⁹

Among the open-shell PAHs, *n*-*peri*-acenes (*n* is the number of outer benzenoid rings along the zigzag direction, Figure 1a), conceptually formed *via* edgewise fusion of two linear acenes, represent the smallest well-defined graphene fragments containing both high-symmetry edge topologies of graphene, *viz.* armchair and zigzag. This makes *peri*-acenes model systems to study the onset and evolution of various exotic physical properties predicted in graphene. Recent years have witnessed a resurgent interest in *peri*-acenes, fueled by theoretical predictions of a substantial decrease in the electronic gap with increasing size,²⁰ a spin-polarized ground state with rapid evolution toward a polyradical state,^{21,22} and half-metallicity under external electric fields.²³ While the smallest members of the *peri*-acene series, namely perylene (*n* = 2)²⁴ and bisanthene (*n* = 3),²⁵ have been known and studied since long, larger members of the series remain elusive. Recent solution synthetic attempts suffered from insolubility and inherent reactivity of *peri*-acenes,²⁶ making

ed previously and *peri*-acenes thus remain a virtually unexplored family of PAHs.

Moreover, since the advent of on-surface synthesis, major efforts have been devoted to harvest additional functionalities from PAHs beyond their inherent properties. Such efforts have primarily manifested in the form of substitutional doping with heteroatoms,²⁹⁻³¹ anchoring of functional groups to the π -system of PAHs³² and covalent linking of functionally distinct PAHs to form heterojunctions.³³ These methods, however, pose significant problems such as loss of functional groups during high-temperature growth conditions³² and arbitrary nature of heterojunction formation, thus compromising the structural and functional integrity of such systems. In this regard, controlled embedment of non-benzenoid ring topologies, that significantly influence the local structural,³⁴⁻³⁶ chemical³⁷ and electronic^{38,39} properties of graphene and PAHs, represents an alternative route to tune the intrinsic properties of graphene-based nanostructures. Non-benzenoid rings, in particular odd-membered rings such as pentagons and heptagons, frequently occur as point and line defects in graphene, where large defect reversal barriers stably sustains them at ambient conditions.⁴⁰ However, such topologies are mostly reported to occur under non-equilibrium conditions, precluding their controlled generation and placement to create functional components. Recent developments in on-surface chemistry have demonstrated viable routes to generate non-benzenoid ring topologies,^{41,42} providing opportunities toward their rational fabrication and characterization.

In this work, we report the on-surface synthesis of two isomeric open-shell PAHs *via* surface-catalyzed cyclodehydrogenation and oxidative ring-closure reactions in combination with STM atom manipulation on Au(111) under UHV conditions: the long-pursued pristine *peri*-tetracene (**1**), and a non-benzenoid non-alternant structural isomer of **1**, namely dibenzo[*a,m*]dicyclohepta[*bcde,nopq*]rubicene (**2**) containing a pair of embedded azulene units (Figure 1b, c). We conducted detailed structural and electronic characterization of **1** and **2** *via* bond-resolved scanning tunneling microscopy (STM) and spectroscopy (STS) at low temperatures ($T = 4.5$ K). Through our studies, we unravel the electronic structure of pristine *peri*-acenes, thus far restricted to theoretical analyses; and elucidate the electronic ramifications of non-benzenoid ring topologies. Furthermore, we reveal **1** and **2** to exhibit one of the lowest electronic gaps reported till date for graphene nanostructures on surfaces. Our experimental results, aided by *ab initio* mean-field theory calculations, not only demonstrate the synthesis and atomic-scale characterization of ultra-low-gap open-shell graphene nanostructures that have eluded modern synthetic chemistry for decades, but also motivate the rational fabrication of larger non-benzenoid ring topologies as functional centers toward the perspective of engineering graphene-based devices.

Results and Discussion

Design and in-solution syntheses of chemical precursors toward on-surface synthesis. Figure 1b, c show

the synthetic route toward **1** and **2**. Our targeted precursor for on-surface synthesis of **1** is 7,14-di-(2-methylphenyl)benzo[*k*]tetracene (**3**), where we expect the methylbenzene substituents to participate in cyclodehydrogenation and oxidative ring-closure reactions upon annealing on Au(111) surface, thus yielding four benzenoid rings and leading to the formation of **1**. The synthesis of **3** was achieved starting from 2',5'-dibromo-2,2''-dimethyl-1,1':4',1''-terphenyl (**S1**)²⁶ in three steps, *via* a Suzuki coupling-deprotection-intramolecular cyclization sequence in a total yield of 18 % (Figure 1b). Similarly, our designed precursor toward on-surface synthesis of **2** is 1,10-dimethyldibenzo[*a,m*]rubicene (**4**), wherein we expect on-surface oxidative ring-closure reactions of the methyl substituents to afford formation of two heptagonal rings in the polycyclic framework, thus leading to the formation of **2**. The synthesis of **4** was started with 5,11-dibromoindeno[1,2-*b*]fluorine-6,12-dione (**S5**)⁴³ through Suzuki coupling and Ramirez reactions, followed by Palladium-catalyzed intramolecular ring-closing and subsequent debromination in four steps, with a total yield of 17% (Figure 1c). All compounds were characterized by NMR analysis and mass spectroscopy, and additional elemental analysis for **3** and **4** are provided in the supporting information.

On-surface synthesis and characterization of *peri*-tetracene(1**).** After sublimation of submonolayer quantities of **3** under UHV conditions onto an atomically clean Au(111) surface held at room temperature, large-scale STM images (Figure 2a) show the predominant presence of large self-assembled islands and chain-like structures, as well as sporadically distributed individual molecules (see Figure S1 for high-resolution STM images of the room temperature phase of **3**). A high-resolution STM image of an individual molecule (inset, Figure 2a) reveals the presence of two prominent lobes with an apparent height of ~ 2.9 Å, ascribed to the methylbenzene moieties that bend in an out-of-plane fashion against the benzo[*k*]tetracene backbone (Figure S1). Annealing the sample to 300°C results in notable changes in the surface topography. Large-scale STM images (Figure 2b) show an absence of self-assembled structures, with isolated molecules and small clusters present on the surface. About 21% of the molecules (statistics for 206 molecules) present on the surface exhibit a distinctive rectangular topography with a uniform apparent height of ~ 1.9 Å (referred to as **1**), suggesting it to be the result of complete ring-closure reactions of **3** (Figure 2b, highlighted with a white circle). However, the exact chemical identity of **1** is difficult to identify *via* conventional STM imaging alone, which fundamentally probes the local density of states near the Fermi energy, and is therefore insensitive to the total electron density of the molecule which manifests as the chemical structure. To circumvent this limitation, we functionalize the STM tip with a carbon monoxide (CO) molecule to conduct imaging in the regime of Pauli repulsion,^{44,45} yielding the visualization of the chemical structure. Figure 2c shows a high-resolution STM image of **1** acquired with a CO-functionalized tip, wherein at the

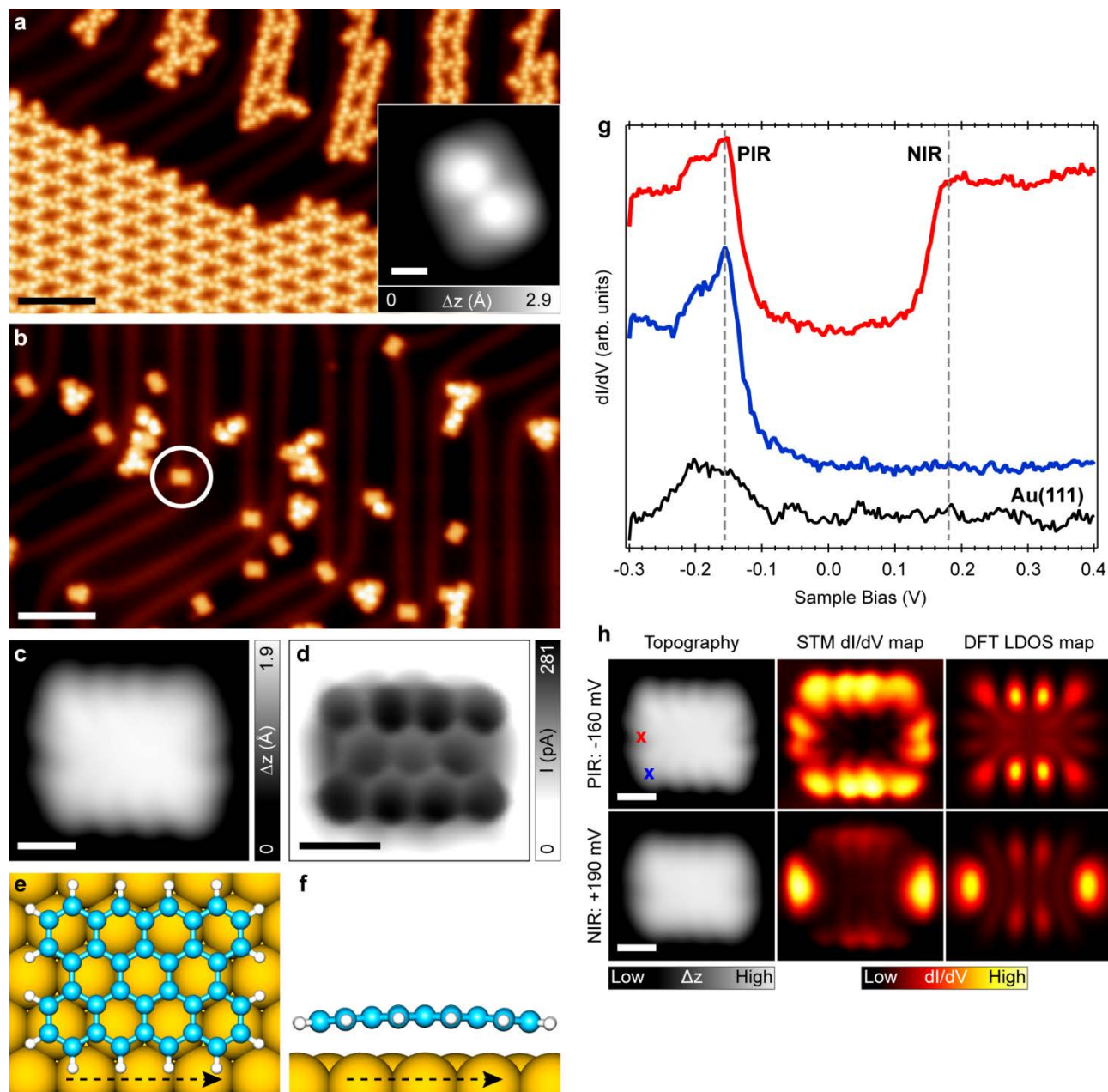


Figure 2. On-surface synthesis and characterization of **1 on Au(111).** (a) Overview STM topography image of the Au(111) surface after room temperature deposition of **3** ($V = -1$ V, $I = 70$ pA). Inset: high-resolution STM image of **3** ($V = -1$ V, $I = 70$ pA). (b) Overview STM topography image of the surface after annealing to 300°C. White circle highlights the molecular species corresponding to **1** ($V = -1$ V, $I = 40$ pA). (c) High-resolution STM image of **1** acquired with a CO-functionalized tip ($V = -160$ mV, $I = 70$ pA). (d) UHR-STM image of **1** evidencing formation of pristine *peri*-tetracene (open feedback parameters: $V = -5$ mV, $I = 50$ pA, $\Delta z = -0.9$ Å). (e), (f) Top and side views of the DFT-optimized equilibrium geometry of **1** on Au(111). The dashed arrows along the long axis of the molecule help interpret the side view – a convention followed in all the figures. (g) dI/dV spectra on **1** (red and blue curves) acquired with a CO-functionalized tip. A reference spectrum on Au(111) is shown in black. The spectra are vertically shifted for clarity. The positions at which the spectra on the molecule were acquired are highlighted in the top-left image in (h) with red and blue crosses. (h) High-resolution STM images (left), simultaneously acquired dI/dV maps (center) and corresponding DFT-calculated LDOS maps (right) at the energetic positions corresponding to the PIR (top) and the NIR (bottom). Open feedback parameters for the dI/dV spectra: $V = -300$ mV, $I = 150$ pA; $V_{\text{rms}} = 8$ mV. Tunneling parameters for the STM images and associated dI/dV maps: PIR – $V = -160$ mV, $I = 100$ pA; $V_{\text{rms}} = 20$ mV; NIR – $V = 190$ mV, $I = 150$ pA; $V_{\text{rms}} = 20$ mV. Scale bars: (a), (b) – 7 nm; inset (a), (c), (d), (h) – 0.5 nm.

chosen tunneling bias voltage (*i.e.* -160 mV) it exhibits rich features in the local density of states (LDOS), particularly noticeable at the peripheries along the long axis of the molecule as four distinct lobes. Finally, the corre-

sponding ultra-high-resolution STM (UHR-STM) image unequivocally establishes **1** to be pristine *peri*-tetracene (Figure 2d, also see Figure S2 for height-dependent UHR-STM images of **1**). The apparent planar conformation of **1**

on Au(111) revealed *via* the UHR-STM image is further verified by density functional theory (DFT) calculations (Figure 2e, f).

We probed the electronic structure of **1** on Au(111) *via* STS (Figure 2g, h). Voltage-dependent differential conductance spectra (dI/dV vs. V) acquired with a CO-functionalized tip on **1** show prominent features in the DOS at -160 mV and 190 mV (Figure 2g). These peaks are assigned to the positive (-160 mV) and the negative (190 mV) ion resonances (PIR and NIR) deriving from the highest occupied and the lowest unoccupied molecular orbitals (HOMO and LUMO) of **1**, respectively (see Figure S3 for STS with a metallic tip). The extracted HOMO-LUMO gap of **1** on Au(111) thus amounts to 350 meV, which is considerably lower in comparison to reported HOMO-LUMO gap values for similar systems; *e.g.* the HOMO-LUMO gap of the hitherto longest on-surface synthesized acene, *i.e.* undecacene on Au(111), was reported to be 1.09 eV.¹³ Figure 2h shows the corresponding STM topography images (left) and the simultaneously acquired dI/dV maps (center) obtained with a CO-functionalized tip at the energetic positions of the PIR (top) and the NIR (bottom) (see Figure S4 for the constant-height dI/dV maps of **1**). The DFT-calculated LDOS maps of the HOMO and the LUMO of **1** (Figure 2h, right), evaluated at a height of 5 Å above the molecular plane, show remarkable agreement with the experimental dI/dV maps. This allows us to infer that the conductance features present in the dI/dV maps can be correlated with the spatial distribution of the probability densities of the corresponding frontier orbital wavefunctions, thereby concluding the electronic structure of **1** on Au(111) (see Figure S5 for the DFT-calculated molecular orbitals of **1**).

On-surface synthesis and characterization of dibenzo[*a,m*]dicyclohepta[*bcde,nopq*]rubicene (2**).** After sublimation of submonolayer quantities of **4** onto an atomically clean Au(111) surface held at room temperature, large-scale STM images (Figure 3a) show the presence of self-assembled linear chains as well as individual molecules (see Figure S6 for high-resolution STM images of the room temperature phase of **4**). A high-resolution STM image of an individual molecule (inset, Figure 3a) reveals the presence of two prominent lobes with an apparent height of ~ 2.5 Å, ascribed to the out-of-plane bending of the methyl groups (Figure S6). After annealing the surface to 300°C, large-scale STM images (Figure 3b) show a marked decrease in the amount of **4**, and various single-molecule products on the surface. We first provide a statistical distribution of the dominant reaction products accounting for 89% of the molecular species present on the surface after annealing at 300°C. A majority of the molecules (58% of 400 molecules) exhibit a two-lobed appearance, and presumably did not undergo ring-closure reactions, corresponding to **4**. About 20% of 400 molecules present only one lobe, possibly corresponding to partial ring-closure reaction of methyl groups to form one heptagonal ring (referred to as **4'**). Notably, there is appearance of a new species (11% of 400 molecules, highlighted with a white circle in Figure 3b) that exhibit a

uniform rectangular topography with an apparent height of ~ 1.9 Å (referred to as **2''**). Figure 3c shows a high-resolution STM image of **2''** acquired with a CO-functionalized tip, revealing sharp ridges at the peripheries along the short axis of the molecule, which is in contrast to the smooth bay-like regions at the peripheries along the long axis of the molecule. Figure 3d shows the corresponding UHR-STM image of **2''** that clearly reveals the non-benzenoid ring topology. While based on the UHR-STM image, it is appealing to ascribe **2''** to the targeted azulene-embedded PAH (Figure 1c), there are particular defining observations that cast doubt over the identity of the molecule. Firstly, during acquisition of the UHR-STM images of **2''** at varying tip-molecule distances, it was found that **2''** moved relatively easily upon approaching the tip closer to the molecule (Figure S7), indicating a weak interaction of **2''** with the surface. Secondly, a careful observation of Figure 3d reveals that the heptagonal rings present a rather elongated appearance with a significant loss of resolution at the apices, which appear remarkably flat. Finally, the heptagonal rings exhibit the weakest contrast among all the rings (*i.e.* draw the least amount of tunneling current). Ring-specific current contrast in molecules sensitively depends on the variation in intramolecular electron density,⁴⁶ which affects the electrostatic potential landscape of the molecule, potentially yielding information on conjugation and aromaticity. The observation of a weak contrast for the heptagonal rings could therefore be an indication of the loss of conjugation within the rings. Since it is ring-closure reactions of methyl groups that entails formation of the heptagonal rings, we speculate that an incomplete dehydrogenation resulting in the loss of only one out of the three hydrogen atoms from each methyl group leads to the saturation of the apical carbon atoms of the heptagonal rings with two hydrogen atoms, thereby imparting a non-conjugated character to the rings. Figure 3e, f show the DFT-optimized equilibrium geometry of **2''**, where the sp^3 configuration of the apical carbon atoms of the heptagonal rings results in a non-planar conformation of the molecule on the surface. To lend support to our speculation, we conducted STS measurements to probe the electronic structure of **2''** (Figure 3g, h). dI/dV spectra on **2''** acquired with a CO-functionalized tip show strong peaks in the DOS at -1.25 V and 1.55 V (Figure 3g), assigned to the PIR and the NIR. Thus, **2''** exhibits a large HOMO-LUMO gap of 2.80 eV on Au(111). Figure 3h shows the corresponding STM topography images (left) and the simultaneously acquired dI/dV maps (center) obtained with a CO-functionalized tip at the energetic positions of the PIR (top) and the NIR (bottom) (see Figure S8 for the constant-height dI/dV maps of **2''**). The DFT-calculated LDOS maps of the HOMO and the LUMO of the molecule (Figure 3h, right), evaluated at a height of 3 Å above the molecular plane, show remarkable agreement with the experimental dI/dV maps, thereby proving our speculation and concluding the identity of **2''**. In addition, identification of **2''** leads now to a straightforward explanation for the identity of the one-lobed species **4'** – the end not exhibiting the lobed feature presents an identical appear-

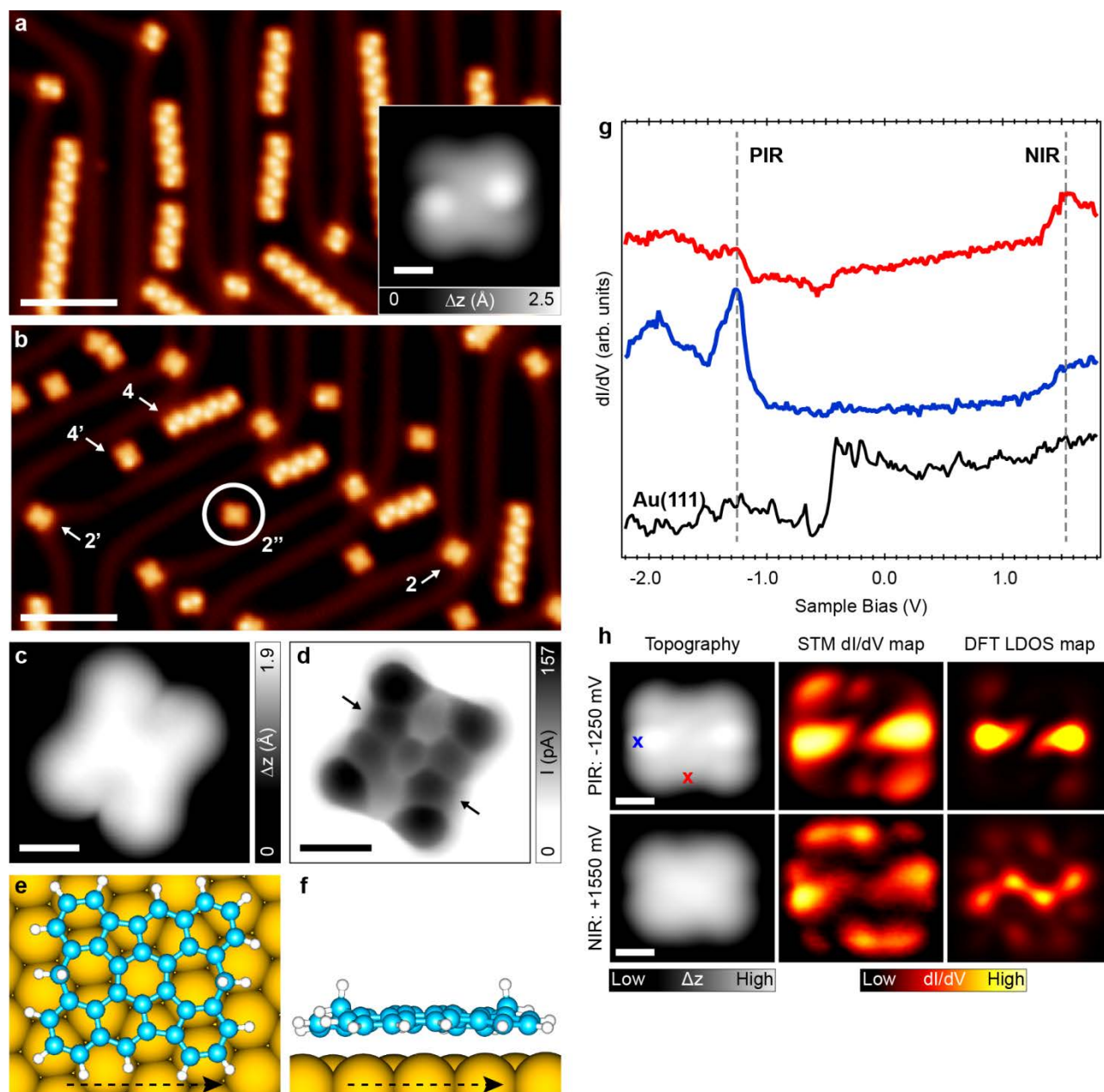


Figure 3. On-surface reactions of 4 and structural and electronic characterization of 2'' on Au(111). (a) Overview STM topography image of the Au(111) surface after room temperature deposition of 4 ($V = -700$ mV, $I = 100$ pA). Inset: high-resolution STM image of 4 ($V = -20$ mV, $I = 100$ pA). (b) Overview STM topography image of the surface after annealing to 300°C. White circle highlights the molecular species corresponding to 2'' ($V = -700$ mV, $I = 100$ pA), with other reaction products labeled with arrows. (c) High-resolution STM image of 2'' acquired with a CO-functionalized tip ($V = -30$ mV, $I = 50$ pA). (d) UHR-STM image of 2'' revealing the non-benzenoid framework (open feedback parameters: $V = -5$ mV, $I = 50$ pA, $\Delta z = -0.5$ Å). The arrows indicate the pentagonal rings on both sides of the molecule. (e), (f) Top and side views of the DFT-optimized equilibrium geometry of 2'' on Au(111). (g) dI/dV spectra on 2'' (red and blue curves) acquired with a CO-functionalized tip. The positions at which the spectra on the molecule were acquired are highlighted in the top-left image in (h) with red and blue crosses. (h) High-resolution STM images (left), simultaneously acquired dI/dV maps (center) and corresponding DFT-calculated LDOS maps (right) at the energetic positions corresponding to the PIR (top) and the NIR (bottom). Open feedback parameters for the dI/dV spectra: $V = -2.20$ V, $I = 200$ pA; $V_{\text{rms}} = 20$ mV. Tunneling parameters for the STM images and associated dI/dV maps: PIR - $V = -1.25$ V, $I = 140$ pA; $V_{\text{rms}} = 20$ mV; NIR - $V = 1.55$ V, $I = 170$ pA; $V_{\text{rms}} = 20$ mV. Scale bars: (a), (b) - 7 nm; inset (a), (c), (d), (h) - 0.5 nm.

ance to 2'', thus corresponding to formation of an unconjugated heptagonal ring consisting of a doubly-hydrogenated apex carbon atom, while the end exhibiting the lobed feature consists of unreacted methyl group.

Having ascertained the identity of 2'', we explored the possibility of generating the targeted fully conjugated species 2 from 2'' by means of STM atom manipulation. Toward this end, we aim to achieve selective cleavage of one hydrogen atom from each of the apical carbon atoms

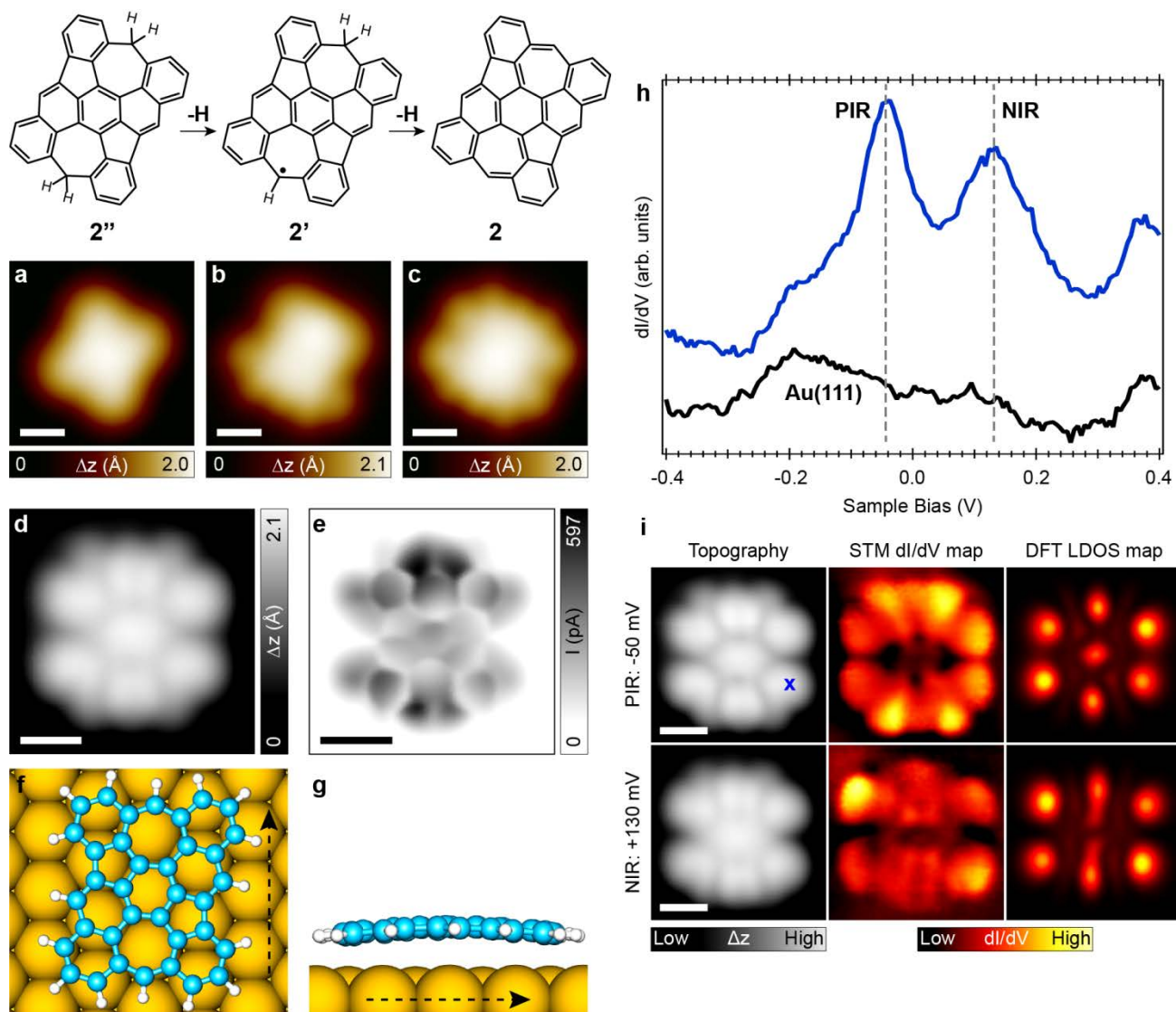


Figure 4. On-surface generation of **2 via STM atom manipulation and its structural and electronic characterization.** (a)-(c) Series of high-resolution STM images and the corresponding chemical structures, showing generation of **2** through voltage-pulse-induced dissociation of individual hydrogen atoms from **2''**; (a) **2''**, containing doubly hydrogenated heptagonal apices, (b) intermediate radical species **2'** generated after dissociation of the first hydrogen atom, (c) generation of **2** after dissociation of the second hydrogen atom. ($V = -100$ mV, $I = 50$ pA). (d) High-resolution STM image of **2** acquired with a CO-functionalized tip ($V = -100$ mV, $I = 50$ pA). (e) UHR-STM image of **2** (open feedback parameters: $V = -5$ mV, $I = 50$ pA, $\Delta z = -0.85$ Å). (f), (g) Top and side views of the DFT-optimized equilibrium geometry of **2** on Au(111). (h) dI/dV spectrum on **2** (blue curve) acquired with a CO-functionalized tip. The position at which the spectrum on the molecule was acquired is highlighted in the top-left image in (i) with a blue cross. (i) High-resolution STM images (left), simultaneously acquired dI/dV maps (center) and corresponding DFT-calculated LDOS maps (right) at the energetic positions corresponding to the PIR (top) and the NIR (bottom). Open feedback parameters for the dI/dV spectra: $V = -400$ mV, $I = 200$ pA; $V_{\text{rms}} = 6$ mV. Tunneling parameters for the STM images and the associated dI/dV maps: PIR - $V = -50$ mV, $I = 150$ pA; $V_{\text{rms}} = 20$ mV; NIR - $V = 120$ mV, $I = 150$ pA; $V_{\text{rms}} = 20$ mV. All scale bars: 0.5 nm.

of the heptagonal rings. To realize this, the STM tip was positioned at the center of **2''** and the feedback loop was opened at the tunneling parameters $V = 100$ mV and $I = 2$ pA. The tip was subsequently retracted by 4.5-5.0 Å to limit the tunneling current. Finally, the tunneling bias voltage was gradually increased to a range between 3.6 and 4.0 V, wherein an abrupt change in the tunneling current was consistently observed, signaling a manipulation event. This bias range is consistent with the C-H bond dissociation energy within the CH_2 groups in 9,10-

dihydroanthracene (3.5 eV),⁴⁷ and previous single dehydrogenation experiments on PAHs with CH_2 moieties.^{15,48} Figure 4a-c demonstrate the manipulation sequence wherein starting from **2''** (Figure 4a), sequential dehydrogenation leads first to the formation of an intermediate radical species **2'** (Figure 4b), and finally to the fully conjugated species **2** (Figure 4c). We found removal of the two hydrogen atoms to be a sequential two-step process for repeated manipulation experiments, possibly related to the limited lifetime of the tunneling electrons for a

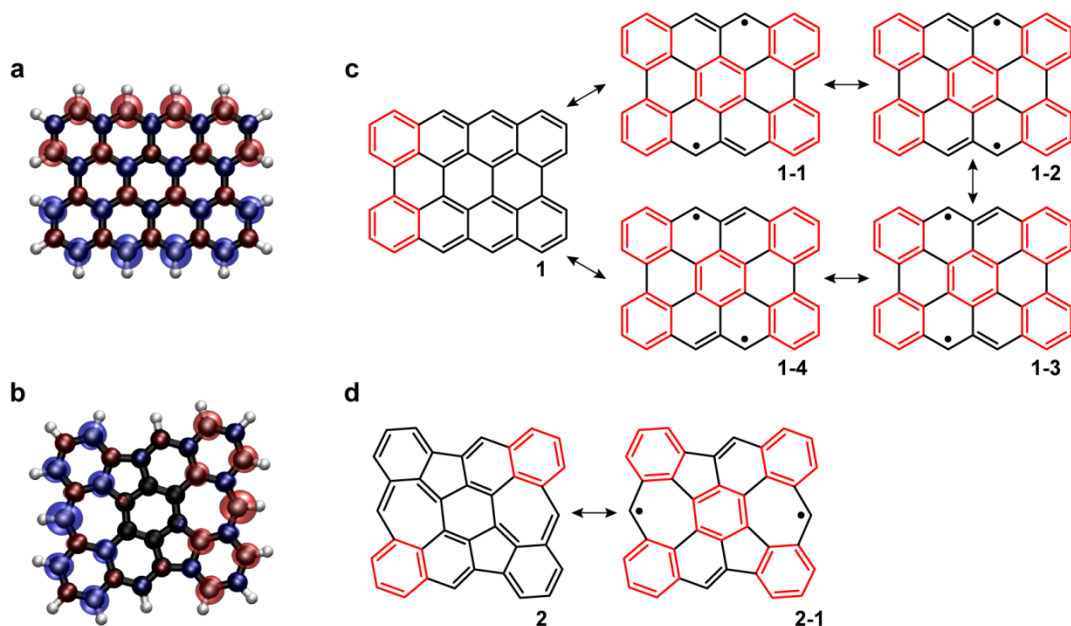


Figure 5. Calculated spin density distributions of **1 and **2** and the relation to Clar’s sextet theory.** (a), (b) DFT-computed spin density distributions of **1** (a) and **2** (b) (spin up: blue, spin down: red). (c), (d) Closed-shell Kekulé and open-shell non-Kekulé resonance structures of **1** (c) and **2** (d). The rings highlighted in red represent Clar sextets.

molecule adsorbed on a metal surface (see Figure S9 and S10 for additional manipulation experiments and elaboration on the identity of **2'**, respectively). Furthermore, upon closer inspection of STM images, we find that among the remaining 11% of minor reaction products after annealing at 300°C that have not been accounted for till now, 8% (out of 400 molecules) corresponds to the intermediate radical species **2'** and 3% corresponds to the desired fully conjugated species **2**, indicating that **2** may also be obtained from thermal annealing of **4** at 300°C, albeit with low yields. While further annealing at 350°C visibly enhances the yield of **2**, such high temperatures unfortunately also promote intermolecular cross-dehydrogenative coupling reactions, leading to the formation of irregular covalently-bonded molecular clusters (Figure S11). We note that optimization of the annealing time and temperatures, and usage of catalytically more active coinage metal surfaces (*e.g.* Ag or Cu), could possibly enhance the yield of **2** on the surface *via* the thermal annealing route.

We next conducted a detailed structural and spectroscopic characterization of **2**. Figure 4d shows a high-resolution STM image of **2** acquired with a CO-functionalized tip, showing rich features in the LDOS at the chosen tunneling bias voltage (*i.e.* -100 mV). The corresponding UHR-STM image (Figure 4e, also see Figure S12 for height-dependent UHR-STM images of **2**) clearly shows the intramolecular features with the non-benzenoid rings. Importantly, the chemical structure of the molecule is strongly convoluted with the LDOS, especially at the apices of the heptagonal rings – a feature absent in the UHR-STM image of **2'** (Figure 3d). Furthermore, the heptagonal rings appear completely undistorted, in contrast to their elongated appearance seen in the case of **2'**. DFT calculations predict that **2** adopts a

planar conformation on Au(111) (Figure 4f, g), evident from the UHR-STM image. Figure 4h, i show the results of the STS measurements on **2**, conducted with a CO-functionalized tip. *dI/dV* spectrum on **2** shows strong peaks in the DOS at -50 mV and 130 mV (Figure 4h, also see Figure S3), assigned to the PIR and the NIR. Thus, **2** exhibits an ultra-low HOMO-LUMO gap of 180 meV on Au(111), a drastic decrease from the corresponding value of 2.80 eV found for **2'** (Figure 3g). This large difference in the electronic gaps of **2** and **2'** can be rationalized through the different degrees of conjugation in the molecules – **2'** is not fully conjugated, whereas **2** is a fully conjugated species. Furthermore, compared to **1**, **2** exhibits a considerable reduction of the HOMO-LUMO gap by almost 50%. Thus, judicious placement of non-benzenoid ring topologies in graphene nanostructures offers a viable route to modulate their fundamental electronic structure. Figure 4i shows the corresponding STM topography images (left) and the simultaneously acquired *dI/dV* maps (center) obtained with a CO-functionalized tip at the energetic positions of the PIR (top) and the NIR (bottom) (see Figure S13 for the constant-height *dI/dV* maps of **2**). The DFT-calculated LDOS maps of the HOMO and the LUMO of **2** (Figure 4i, right), evaluated at a height of 5 Å above the molecular plane, show excellent agreement with the experimental *dI/dV* maps, concluding the electronic structure of **2** on Au(111) (see Figure S14 for the DFT-calculated molecular orbitals of **2**).

Theoretical characterization of the electronic ground states of **1 and **2**.** Investigation of the magnetic structure of PAHs *via* STM remains challenging as a result of the extremely low magnetic anisotropy originating from the intrinsically weak spin-orbit coupling in carbon.⁴⁹ Thus, to gain insight into the open-shell characters of **1** and **2**, we conducted spin-polarized DFT calculations

to evaluate the electronic ground state of the free-standing species. Our calculations favor, for both the species, the (antiferromagnetic) open-shell singlet (AFM) state over the (ferromagnetic) open-shell triplet (FM) and the (non-magnetic) closed-shell (NM) states. Specifically, $E_{AFM,1} < E_{NM,1}$ (62 meV) $< E_{FM,1}$ (92 meV), and $E_{AFM,2} < E_{FM,2}$ (65 meV) $< E_{NM,2}$ (101 meV). Our results are consistent with previous theoretical reports that also found an open-shell singlet ground state for **1** utilizing DFT methods,⁵⁰ and more recently, multireference calculations.^{21,22} Interestingly, the computed spin density distributions of **1** and **2** show a marked difference: the maximum spin density for **1** is located at the zigzag edges with the largest amplitude on the central zigzag carbon atoms (Figure 5a); while for **2**, the maximum spin density is located at the apical carbon atoms of the heptagonal rings (Figure 5b). A simple consideration of Clar’s sextet rule⁵¹ elucidates this difference. Both **1** and **2** contain two aromatic sextets in their Kekulé structures, which can be expanded to a maximum of five sextets in the respective non-Kekulé biradical structure(s), leading to a gain in the aromatic stabilization energy, with the formal loss of a π -bond resulting in two unpaired electrons (Figure 5c, d). For **1**, four non-Kekulé resonance structures can be drawn (**1-1** to **1-4** in Figure 5c), wherein the unpaired electrons are located at the four central zigzag carbon atoms; while for **2**, only a single non-Kekulé structure exists (**2-1** in Figure 5d), with the unpaired electrons located at the apical carbon atoms of the heptagonal rings.

Conclusions

We have demonstrated the synthesis of two challenging isomeric open-shell nanographenes, namely, pristine *peri*-tetracene (**1**) and its non-benzenoid non-alternant structural isomer, dibenzo[*a,m*]dicyclohepta[*bcde,nopq*]rubicene (**2**) containing multiple odd-membered rings, through cyclodehydrogenation and oxidative ring-closure reactions, in combination with STM single-atom manipulation on Au(111) surface. The synthesis of *peri*-acenes, long-pursued in organic chemistry, represents an important development toward investigation of spin-polarized edge states at the single-molecule level. Our experiments elucidate the electronic structure of pristine *peri*-acenes at the atomic scale, which has thus far been restricted to theoretical studies. Controlled embedment of non-benzenoid ring topologies, representing an alternative route toward implementing a wide spectrum of functionalities in polyaromatic frameworks, is exemplified through the synthesis of **2**; wherein oxidative ring-closure reactions of methyl groups attached to a dibenzo[*a,m*]rubicene core affords formation of heptagonal rings. Scanning tunneling spectroscopy measurements revealed ultra-low electronic gaps for both species, motivating their use as functional components in organic electronics, for example as metal-semiconductor interconnects in graphene-nanoribbon-based field effect transistors. Importantly, the electronic gap of **2** (*i.e.* 180 meV) is about 50% lower than that for **1** (*i.e.* 350 meV), demonstrating that incorporation of non-benzenoid ring topologies (here, azulene moieties) in a

polybenzenoid framework offers a route to establish control over electronic structure of PAHs. Spin-polarized density functional theory calculations predict both species to exhibit an open-shell singlet ground state, making them promising candidates for spintronic applications. We propose to incorporate these systems, *via* on-surface Ullmann reaction, in one- and two-dimensional lattices to study spin coupling between neighboring molecules – representing ideal platforms toward investigation of low-dimensional magnetism in organic nanostructures, and future spin-based information storage and computation.

Methods

Sample preparation and STM measurements. STM measurements were performed with a commercial low-temperature STM from Scienta Omicron operating at base pressures below 1×10^{-10} mbar. Au(111) single crystal surface was prepared *via* iterated cycles of sputtering with Ar⁺ ions at $p = 6 \times 10^{-6}$ mbar, and annealing to 750 K for 30 minutes at pressures below 5×10^{-10} mbar. Prior to the deposition of molecules, STM was used to check the quality and cleanliness of the surface. Precursor molecules **3** and **4** were sublimed at 400 K and 500 K, respectively, on Au(111) surface held at room temperature. All STM images were acquired in constant-current mode unless otherwise stated. Indicated tunneling bias voltages are given with respect to the sample. Unless otherwise stated, gold-coated tungsten tips were used for STM imaging and spectroscopy. Constant-height differential conductance spectra and dI/dV maps were acquired using the lock-in technique to obtain a signal proportional to dI/dV from the first harmonic of the tunneling current ($f = 860$ Hz). UHR-STM images were acquired in constant-height mode with a CO-functionalized tip, at biases close to the Fermi energy, and the current signal was recorded. Open feedback parameters and subsequent lowering of the tip height (*i.e.* Δz) are provided in the figure captions. CO-functionalized tips were obtained by picking up individual CO molecules from NaCl islands, deposited after completion of the reaction steps, since NaCl islands greatly facilitate identification and pickup of CO molecules. All STM and dI/dV images were processed and analyzed with WSxM software.⁵²

Calculation Methods. To obtain the equilibrium geometries of the molecules adsorbed on Au(111) substrate and to compute the corresponding STM images, we used the CP2K code⁵³ implementing DFT within a mixed Gaussian plane waves approach.⁵⁴ The surface/adsorbate systems were modeled within the repeated slab scheme, *i.e.* a simulation cell contained 4 atomic layers of Au along the [111] direction and a layer of hydrogen atoms to passivate one side of the slab in order to suppress one of the two Au(111) surface states. 40 Å of vacuum was also included in the simulation cell to decouple the system from its periodic replicas in the direction perpendicular to the surface. The electronic states were expanded with a TZV2P Gaussian basis set for C and H species and a DZVP basis set for Au species. A cutoff of 600 Ry was used for the plane wave basis set. Norm-conserving Goedecker-Teter-Hutter pseudopotentials were used to represent the

frozen core electrons of the atoms.⁵⁵ We used the PBE parameterization for the generalized gradient approximation of the exchange correlation functional.⁵⁶ To account for van der Waals interactions, we used the scheme proposed by Grimme.⁵⁷ We considered supercells of 41.27 x 40.85 Å corresponding to 224 surface units. To obtain the equilibrium geometries, we kept the atomic positions of the bottom two layers of the slab fixed to the ideal bulk positions, and all other atoms were relaxed until forces were lower than 0.005 eV/Å. To obtain simulated STM images within the Tersoff-Hamann approximation,^{58,59} we extrapolated the electronic orbitals to the vacuum region in order to correct the wrong decay of the charge density in vacuum due to the localized basis set.⁵⁹ LDOS maps were simulated with an *s*-wave tip model. Energies of the equilibrium gas-phase geometries of the molecules for the non-magnetic, ferromagnetic and antiferromagnetic electronic configurations were obtained with QUANTUM ESPRESSO.⁶⁰ The PBE approximation for the exchange correlation functional was used, pseudopotentials from the Standard Solid State Pseudopotentials (SSSP) library⁶¹ were used to model the ionic potential and a cutoff of 50 (400) Ry was employed for the plane wave expansion of the orbitals (charge density).

ASSOCIATED CONTENT

Supporting Information. Details on synthesis and characterization of **3** and **4**, additional STM and STS data, height-dependent UHR-STM images and additional DFT calculations. This material is available free of charge via the Internet at <http://pubs.acs.org>.

Financial Interest Statement. The authors declare no competing financial interests.

AUTHOR INFORMATION

Corresponding Author

*xinliang.feng@tu-dresden.de

*roman.fasel@empa.ch

Author Contributions

[†]S.M. and T.G.L. contributed equally. K.M., X.F., P.R. and R.F. conceived the work. T.G.L., J.L. and R.B. designed, synthesized and characterized the precursor molecules. S.M. performed the on-surface synthesis and scanning tunneling microscopy experiments. C.A.P. performed the theoretical calculations. S.M. wrote the manuscript with contributions from all co-authors.

ACKNOWLEDGMENT

We acknowledge the Swiss National Science Foundation and the NCCR MARVEL funded by the Swiss National Science Foundation, the European Union's Horizon 2020 research and innovation programme under grant agreement number 785219 (Graphene Flagship Core 2), DFG-NSFC Joint Sino-German Research Project (EnhanceNano), Center for Advancing Electronics Dresden (cfaed), the European Social Fund and the Federal State of Saxony (ESF-Project GRAPHD, TU Dresden) for financial support. Computational support from the Swiss Supercomputing Center (CSCS) and PRACE project 2016153518 is gratefully acknowledged. T.G.L. gratefully

acknowledges the International Excellence Graduate School on Emerging Materials and Processes Korea (iEGSEMP Korea) in the context of TU Dresden's institutional strategy *The Synergetic University*. We thank Kristjan Eimre for his help with DFT simulations and fruitful scientific discussions.

REFERENCES

- (1) Fujita, M.; Wakabayashi, K.; Nakada, K.; Kusakabe, K. Peculiar Localized State at Zigzag Graphite Edge. *J. Phys. Soc. Jpn.* **1996**, *65*, 1920–1923.
- (2) Pisani, L.; Chan, J. A.; Montanari, B.; Harrison, N. M. Electronic Structure and Magnetic Properties of Graphitic Ribbons. *Phys. Rev. B* **2007**, *75*, 064418.
- (3) Wang, W. L.; Yazyev, O. V.; Meng, S.; Kaxiras, E. Topological Frustration in Graphene Nanoflakes: Magnetic Order and Spin Logic Devices. *Phys. Rev. Lett.* **2009**, *102*, 157201.
- (4) Morita, Y.; Suzuki, S.; Sato, K.; Takui, T. Synthetic Organic Spin Chemistry for Structurally Well-Defined Open-Shell Graphene Fragments. *Nat. Chem.* **2011**, *3*, 197–204.
- (5) Ge, Y.; Ji, J.; Shen, Z.; Zhang, Q.; Jian, A.; Duan, Q.; Wang, C.; Jiang, J.; Zhang, W.; Sang, S. First Principles Study of Magnetism Induced by Topological Frustration of Bowtie-Shaped Graphene Nanoflake. *Carbon* **2018**, *127*, 432–436.
- (6) Yazyev, O. V. Emergence of Magnetism in Graphene Materials and Nanostructures. *Rep. Prog. Phys.* **2010**, *73*, 056501.
- (7) Nakano, M.; Champagne, B. Nonlinear Optical Properties in Open-Shell Molecular Systems. *Wiley Interdiscip. Rev. Comput. Mol. Sci.* **2016**, *6*, 198–210.
- (8) Smith, M. B.; Michl, J. Singlet Fission. *Chem. Rev.* **2010**, *110*, 6891–6936.
- (9) Ruffieux, P.; Wang, S.; Yang, B.; Sánchez-Sánchez, C.; Liu, J.; Dienel, T.; Talirz, L.; Shinde, P.; Pignedoli, C. A.; Passerone, D.; Dumslaff, T.; Feng, X.; Müllen, K.; Fasel, R. On-Surface Synthesis of Graphene Nanoribbons with Zigzag Edge Topology. *Nature* **2016**, *531*, 489–492.
- (10) Urgel, J. I.; Hayashi, H.; Di Giovannantonio, M.; Pignedoli, C. A.; Mishra, S.; Deniz, O.; Yamashita, M.; Dienel, T.; Ruffieux, P.; Yamada, H.; Fasel, R. On-Surface Synthesis of Heptacene Organometallic Complexes. *J. Am. Chem. Soc.* **2017**, *139*, 11658–11661.
- (11) Tönshoff, C.; Bettinger, H. F. Photogeneration of Octacene and Nonacene. *Angew. Chem. Int. Ed.* **2010**, *49*, 4125–4128.
- (12) Krüger, J.; García, F.; Eisenhut, F.; Skidin, D.; Alonso, J. M.; Guitián, E.; Pérez, D.; Cuniberti, G.; Moresco, F.; Peña, D. Decacene: On-Surface Generation. *Angew. Chem. Int. Ed.* **2017**, *56*, 11945–11948.
- (13) Zuzak, R.; Dorel, R.; Kolmer, M.; Szymonski, M.; Godlewski, S.; Echavarren, A. M. Higher Acenes by On-Surface Dehydrogenation: From Heptacene to Undecacene. *Angew. Chem. Int. Ed.* **2018**, *57*, 10500–10505.
- (14) Konishi, A.; Hirao, Y.; Matsumoto, K.; Kurata, H.; Kishi, R.; Shigeta, Y.; Nakano, M.; Tokunaga, K.; Kamada, K.; Kubo, T. Synthesis and Characterization of Quarteranthene: Elucidating the Characteristics of the Edge State of Graphene Nanoribbons at the Molecular Level. *J. Am. Chem. Soc.* **2013**, *135*, 1430–1437.
- (15) Pavliček, N.; Mistry, A.; Majzik, Z.; Moll, N.; Meyer, G.; Fox, D. J.; Gross, L. Synthesis and Characterization of Triangulene. *Nat. Nanotechnol.* **2017**, *12*, 308–311.

- (16) Alcón, I.; Viñes, F.; Moreira, I. de P. R.; Bromley, S. T. Existence of Multi-Radical and Closed-Shell Semiconducting States in Post-Graphene Organic Dirac Materials. *Nat. Commun.* **2017**, *8*, 1957.
- (17) Wu, S.; Li, M.; Phan, H.; Wang, D.; Herng, T. S.; Ding, J.; Lu, Z.; Wu, J. Toward Two-Dimensional π -Conjugated Covalent Organic Radical Frameworks. *Angew. Chem. Int. Ed.* **2018**, *57*, 8007–8011.
- (18) Jiang, D.; Sumpter, B. G.; Dai, S. Unique Chemical Reactivity of a Graphene Nanoribbon's Zigzag Edge. *J. Chem. Phys.* **2007**, *126*, 134701.
- (19) *On-Surface Synthesis*; Gourdon, A., Ed.; Springer International Publishing: Cham, **2016**.
- (20) Jiang, D.; Dai, S. Circumacenes versus Periacenes: HOMO–LUMO Gap and Transition from Nonmagnetic to Magnetic Ground State with Size. *Chem. Phys. Lett.* **2008**, *466*, 72–75.
- (21) Plasser, F.; Pasalic, H.; Gerzabek, M. H.; Libisch, F.; Reiter, R.; Burgdörfer, J.; Müller, T.; Shepard, R.; Lischka, H. The Multiradical Character of One- and Two-Dimensional Graphene Nanoribbons. *Angew. Chem. Int. Ed.* **2013**, *52*, 2581–2584.
- (22) Mizukami, W.; Kurashige, Y.; Yanai, T. More π Electrons Make a Difference: Emergence of Many Radicals on Graphene Nanoribbons Studied by *Ab Initio* DMRG Theory. *J. Chem. Theory Comput.* **2013**, *9*, 401–407.
- (23) Hod, O.; Barone, V.; Scuseria, G. E. Half-Metallic Graphene Nanodots: A Comprehensive First-Principles Theoretical Study. *Phys. Rev. B* **2008**, *77*, 035411.
- (24) Scholl, R.; Seer, C.; Weitzenböck, R. Perylen, Ein Hoch Kondensierter Aromatischer Kohlenwasserstoff $C_{20}H_{12}$. *Berichte Dtsch. Chem. Ges.* **1910**, *43*, 2202–2209.
- (25) Clar, E. Synthesen von Benzologen des Perylens und Bisanthens. *Chem. Ber.* **1949**, *82*, 46–60.
- (26) Liu, J.; Ravat, P.; Wagner, M.; Baumgarten, M.; Feng, X.; Müllen, K. Tetrabenzo[a,f,j,o]Perylene: A Polycyclic Aromatic Hydrocarbon With An Open-Shell Singlet Biradical Ground State. *Angew. Chem. Int. Ed.* **2015**, *54*, 12442–12446.
- (27) Ajayakumar, M. R.; Fu, Y.; Ma, J.; Hennersdorf, F.; Komber, H.; Weigand, J. J.; Alfonsov, A.; Popov, A. A.; Berger, R.; Liu, J.; Müllen, K.; Feng, X. Toward Full Zigzag-Edged Nanographenes: Peri-Tetracene and Its Corresponding Circumanthracene. *J. Am. Chem. Soc.* **2018**, *140*, 6240–6244.
- (28) Rogers, C.; Chen, C.; Pedramrazi, Z.; Omrani, A. A.; Tsai, H.-Z.; Jung, H. S.; Lin, S.; Crommie, M. F.; Fischer, F. R. Closing the Nanographene Gap: Surface-Assisted Synthesis of Peripentacene from 6,6'-Bipentacene Precursors. *Angew. Chem. Int. Ed.* **2015**, *54*, 15143–15146.
- (29) Bronner, C.; Stremlau, S.; Gille, M.; Brauß, F.; Haase, A.; Hecht, S.; Tegeder, P. Aligning the Band Gap of Graphene Nanoribbons by Monomer Doping. *Angew. Chem. Int. Ed.* **2013**, *52*, 4422–4425.
- (30) Cloke, R. R.; Marangoni, T.; Nguyen, G. D.; Joshi, T.; Rizzo, D. J.; Bronner, C.; Cao, T.; Louie, S. G.; Crommie, M. F.; Fischer, F. R. Site-Specific Substitutional Boron Doping of Semiconducting Armchair Graphene Nanoribbons. *J. Am. Chem. Soc.* **2015**, *137*, 8872–8875.
- (31) Kawai, S.; Saito, S.; Osumi, S.; Yamaguchi, S.; Foster, A. S.; Spijker, P.; Meyer, E. Atomically Controlled Substitutional Boron-Doping of Graphene Nanoribbons. *Nat. Commun.* **2015**, *6*, 8098.
- (32) Carbonell-Sanromà, E.; Hieulle, J.; Vilas-Varela, M.; Brandimarte, P.; Iraola, M.; Barragán, A.; Li, J.; Abadia, M.; Corso, M.; Sánchez-Portal, D.; Peña, D.; Pascual, J. I. Doping of Graphene Nanoribbons *via* Functional Group Edge Modification. *ACS Nano* **2017**, *11*, 7355–7361.
- (33) Cai, J.; Pignedoli, C. A.; Talirz, L.; Ruffieux, P.; Söde, H.; Liang, L.; Meunier, V.; Berger, R.; Li, R.; Feng, X.; Müllen, K.; Fasel, R. Graphene Nanoribbon Heterojunctions. *Nat. Nanotechnol.* **2014**, *9*, 896–900.
- (34) Kawasumi, K.; Zhang, Q.; Segawa, Y.; Scott, L. T.; Itami, K. A Grossly Warped Nanographene and the Consequences of Multiple Odd-Membered-Ring Defects. *Nat. Chem.* **2013**, *5*, 739–744.
- (35) Robertson, A. W.; He, K.; Kirkland, A. I.; Warner, J. H. Inflating Graphene with Atomic Scale Blisters. *Nano Lett.* **2014**, *14*, 908–914.
- (36) Mishra, S.; Krzeszewski, M.; Pignedoli, C. A.; Ruffieux, P.; Fasel, R.; Gryko, D. T. On-Surface Synthesis of a Nitrogen-Embedded Buckybowl with Inverse Stone-Thrower–Wales Topology. *Nat. Commun.* **2018**, *9*, 1714.
- (37) Cretu, O.; Krasheninnikov, A. V.; Rodríguez-Manzo, J. A.; Sun, L.; Nieminen, R. M.; Banhart, F. Migration and Localization of Metal Atoms on Strained Graphene. *Phys. Rev. Lett.* **2010**, *105*, 196102.
- (38) Terrones, H.; Terrones, M.; Hernández, E.; Grobert, N.; Charlier, J.-C.; Ajayan, P. M. New Metallic Allotropes of Planar and Tubular Carbon. *Phys. Rev. Lett.* **2000**, *84*, 1716–1719.
- (39) Lahiri, J.; Lin, Y.; Bozkurt, P.; Oleynik, I. I.; Batzill, M. An Extended Defect in Graphene as a Metallic Wire. *Nat. Nanotechnol.* **2010**, *5*, 326–329.
- (40) Banhart, F.; Kotakoski, J.; Krasheninnikov, A. V. Structural Defects in Graphene. *ACS Nano* **2011**, *5*, 26–41.
- (41) Hieulle, J.; Carbonell-Sanromà, E.; Vilas-Varela, M.; Garcia-Lekue, A.; Guitián, E.; Peña, D.; Pascual, J. I. On-Surface Route for Producing Planar Nanographenes with Azulene Moieties. *Nano Lett.* **2018**, *18*, 418–423.
- (42) Di Giovannantonio, M.; Urgel, J. I.; Beser, U.; Yakutovich, A. V.; Wilhelm, J.; Pignedoli, C. A.; Ruffieux, P.; Narita, A.; Müllen, K.; Fasel, R. On-Surface Synthesis of Indenofluorene Polymers by Oxidative Five-Membered Ring Formation. *J. Am. Chem. Soc.* **2018**, *140*, 3532–3536.
- (43) Rose, B. D.; Maria, P. J. S.; Fix, A. G.; Vonnegut, C. L.; Zakharov, L. N.; Parkin, S. R.; Haley, M. M. Scalable Synthesis of 5,11-Diethynylated Indeno[1,2-b]Fluorene-6,12-Diones and Exploration of Their Solid State Packing. *Beilstein J. Org. Chem.* **2014**, *10*, 2122–2130.
- (44) Weiss, C.; Wagner, C.; Kleimann, C.; Rohlfing, M.; Tautz, F. S.; Temirov, R. Imaging Pauli Repulsion in Scanning Tunneling Microscopy. *Phys. Rev. Lett.* **2010**, *105*, 086103.
- (45) Kichin, G.; Weiss, C.; Wagner, C.; Tautz, F. S.; Temirov, R. Single Molecule and Single Atom Sensors for Atomic Resolution Imaging of Chemically Complex Surfaces. *J. Am. Chem. Soc.* **2011**, *133*, 16847–16851.
- (46) Dienel, T.; Kawai, S.; Söde, H.; Feng, X.; Müllen, K.; Ruffieux, P.; Fasel, R.; Gröning, O. Resolving Atomic Connectivity in Graphene Nanostructure Junctions. *Nano Lett.* **2015**, *15*, 5185–5190.
- (47) Bordwell, F. G.; Cheng, J. P.; Satish, A. V.; Twyman, C. L. Acidities and Homolytic Bond Dissociation Energies (BDEs) of Benzyl-Type Carbon-Hydrogen Bonds in Sterically Congested Substrates. *J. Org. Chem.* **1992**, *57*, 6542–6546.
- (48) Majzik, Z.; Pavliček, N.; Vilas-Varela, M.; Pérez, D.; Moll, N.; Guitián, E.; Meyer, G.; Peña, D.; Gross, L. Studying an Antiaromatic Polycyclic Hydrocarbon Adsorbed on Different Surfaces. *Nat. Commun.* **2018**, *9*, 1198.

- (49) Yazyev, O. V.; Katsnelson, M. I. Magnetic Correlations at Graphene Edges: Basis for Novel Spintronics Devices. *Phys. Rev. Lett.* **2008**, *100*, 047209.
- (50) Jiang, D.; Sumpter, B. G.; Dai, S. First Principles Study of Magnetism in Nanographenes. *J. Chem. Phys.* **2007**, *127*, 124703.
- (51) Clar, E. *The Aromatic Sextet*; Wiley: New York, **1972**.
- (52) Horcas, I.; Fernández, R.; Gómez-Rodríguez, J. M.; Colchero, J.; Gómez-Herrero, J.; Baro, A. M. WSXM: A Software for Scanning Probe Microscopy and a Tool for Nanotechnology. *Rev. Sci. Instrum.* **2007**, *78*, 013705.
- (53) Hutter, J.; Iannuzzi, M.; Schiffmann, F.; Vandevondele, J. CP2K: Atomistic Simulations of Condensed Matter Systems. *Wiley Interdiscip. Rev. Comput. Mol. Sci.* **2014**, *4*, 15–25.
Available at: <https://www.cp2k.org>.
- (54) VandeVondele, J.; Krack, M.; Mohamed, F.; Parrinello, M.; Chassaing, T.; Hutter, J. Quickstep: Fast and Accurate Density Functional Calculations Using a Mixed Gaussian and Plane Waves Approach. *Comput. Phys. Commun.* **2005**, *167*, 103–128.
- (55) Goedecker, S.; Teter, M.; Hutter, J. Separable Dual-Space Gaussian Pseudopotentials. *Phys. Rev. B* **1996**, *54*, 1703–1710.
- (56) Perdew, J. P.; Burke, K.; Ernzerhof, M. Generalized Gradient Approximation Made Simple. *Phys. Rev. Lett.* **1996**, *77*, 3865–3868.
- (57) Grimme, S.; Antony, J.; Ehrlich, S.; Krieg, H. A Consistent and Accurate *Ab Initio* Parametrization of Density Functional Dispersion Correction (DFT-D) for the 94 Elements H-Pu. *J. Chem. Phys.* **2010**, *132*, 154104.
- (58) Tersoff, J. D.; Hamann, D. R. Theory of the Scanning Tunneling Microscope. *Phys. Rev. B* **1985**, *31*, 805–813.
- (59) Tersoff, J. D. Method for the Calculation of Scanning Tunneling Microscope Images and Spectra. *Phys. Rev. B* **1989**, *40*, 11990–11993.
- (60) Giannozzi, P.; Baroni, S.; Bonini, N.; Calandra, M.; Car, R.; Cavazzoni, C.; Ceresoli, D.; Chiarotti, G. L.; Cococcioni, M.; Dabo, I.; Corso, A. D.; de Gironcoli, S.; Fabris, S.; Fratesi, G.; Gebauer, R.; Gerstmann, U.; Gougoussis, C.; Kokalj, A.; Lazzeri, M.; Martin-Samos, L. et al. QUANTUM ESPRESSO: A Modular and Open-Source Software Project for Quantum Simulations of Materials. *J. Phys. Condens. Matter* **2009**, *21*, 395502.
- (61) Lejaeghere, K.; Bihlmayer, G.; Björkman, T.; Blaha, P.; Blügel, S.; Blum, V.; Caliste, D.; Castelli, I. E.; Clark, S. J.; Corso, A. D.; de Gironcoli, S.; Deutsch, T.; Dewhurst, J. K.; Marco, I. D.; Draxl, C.; Dułak, M.; Eriksson, O.; Flores-Livas, J. A.; Garrity, K. F.; Genovese, L. et al. Reproducibility in Density Functional Theory Calculations of Solids. *Science* **2016**, *351*, 1–11.
Available at: <https://molmod.ugent.be/deltacodesdft>.

Table of Contents artwork

